Estimating the Location of Turbulent Layers via Horizontal-Path Laser Tomography

Victor Vilnrotter* and Erkin Sidick†

ABSTRACT. — Laser beams propagating through the atmosphere are impacted by turbulence, which may cause random beam-steering and phase-front distortions that deteriorate the quality of the transmitted beam. Random beam-steering is particularly serious in ground-to-space communications applications, where a small error in the direction vector of the transmitted beam close to the ground may result in a large displacement at the spacecraft, causing deep fades that degrade communications performance. It is therefore important to compensate for beam-steering and higher-order distortions as the beam propagates through the atmosphere. This can be accomplished by using the downlink signal transmitted by the spacecraft as a reference to help characterize the main components of atmospheric turbulence at various distances from the transmitter along the line of sight, thus reducing the effects of beam-steering and higher-order distortions at the spacecraft. This paper describes and experimentally demonstrates a system concept that identifies two or more turbulent layers along a horizontal path and determines their distance, and can be expanded in the future to characterize wavefront distortions caused by each layer.

I. Introduction

The main goal of the horizontal-path Adaptive Optics tomography experiment carried out at the JPL Mesa Antenna Test Range between January and June 2023 was to demonstrate a practical technique for identifying the location of natural or artificial turbulent layers and to characterize these layers in terms of phase error statistics. A secondary goal was to demonstrate the ability to identify and characterize two or more turbulent layers at different distances along the same optical path, as required for compensating multiple turbulent layers impacting the downlink reference signal.

The motivation for measuring the distance to various turbulent layers along the line of sight (LOS) is that deep space optical communications systems incur large point-ahead angles that cannot be easily accommodated by conventional Adaptive Optics compensation systems. This is because the uplink beam propagates outside of the iso-kinetic angle in typical uplink applications. However, a downlink plane-wave entering a

* Communications Architectures and Research Section.

† Formerly with Optics Section.

The research described in this publication was carried out by the Jet Propulsion Laboratory, California Institute of Technology, under a contract with the National Aeronautics and Space Administration (80NM0018D0004).

large receiver aperture could serve as a reference for compensating a narrow uplink beam as it propagates through multiple layers of atmospheric turbulence.

For example, turbulence in an upper layer $z_1 = 10$ km above a receiver with diameter $D = 1$ m that generates a peak-to-null displacement of 1 beamwidth root-mean-squared (RMS) tip-tilt error at a wavelength of $\lambda = 1$ μm will only displace a downlink ray by roughly $\lambda z_1 / D \cong (10^{-6})(10^4) / 1 = 1$ cm when the spacecraft is directly overhead. This implies that only rays passing through the receiver aperture within a 1.01 m disk projected onto the upper turbulent layer at 10 km altitude pass through the receiver aperture; hence, we can approximate the significant region over any turbulent layer as the projection of the telescope aperture onto the turbulent layer along the LOS vector.

With large point-ahead angles, the smaller diameter uplink beam intersects the turbulent layers with different radial displacement at different altitudes; therefore, it is necessary to determine both the distance along the LOS and the location of the radially displaced conjugate plane corresponding to the overlap between uplink beam and the projection of the receiving aperture along the downlink propagation vector. The range measurement along the receiver LOS can be accomplished by placing a wavefront sensor (WFS) at the conjugate planes of the overlap region and measuring the distance between the exit pupil of the receiving telescope via the technique described and evaluated in the following sections. Although these experiments were carried out over a horizontal path, the basic concepts apply to more realistic scenarios at different elevation angles, as would be required for operational deep space optical communications.

II. Optical System Analysis

A. Conjugate Plane of Turbulent Atmospheric Layer

The horizontal-path experiment setup consisted of a 650-nm laser beam nominally collimated by a 106-mm refractor telescope propagating to a 125-mm objective diameter Celestron Schmidt-Cassegrain telescope equipped with a flip-mirror assembly and an eyepiece that generates the exit pupil (i.e., the image of the telescope aperture or more specifically the surface of the correcting plate). This was followed by a high-speed Thorlabs WFS that samples the phase distribution across either the conjugate pupil plane, representing a demagnified image of the telescope aperture called the exit pupil, or the conjugate plane of a turbulent layer, depending on where the WFS is placed along the optical axis.

The design of the optical system for the JPL Mesa experiments is based on the tomography concept shown in Figure 1 (Figure 3 in [1]), which describes the phase and amplitude distribution along the normal to the propagation axis of the illuminating laser field. Figure 1a shows the location of the exit pupil, which is the demagnified image of the telescope aperture, and Figure 1b shows the configuration for reimaging the optical phase-front of the turbulent layer a distance z_1 in front of the telescope objective.

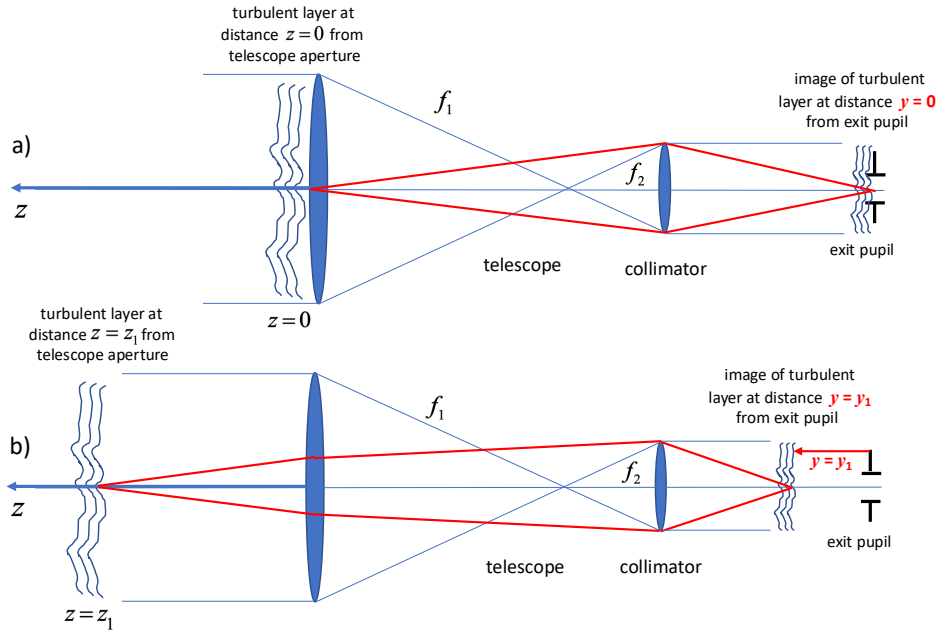

Figure 1. Configurations for a) conjugate pupil plane of the telescope, also known as the exit pupil and b) conjugate plane of turbulent layer in front of the aperture (based on Figure 3 in [1]).

In Figure 1a, the red lines represent rays from a differential area of the optical field (i.e., a point-source) located at the telescope aperture imaged by the second lens (eyepiece) at the telescope's exit pupil, forming an image of the optical field at the aperture. Similarly, a differential area of the optical field just after passing through the turbulent layer is imaged between the exit pupil and the eyepiece, as shown by the rays (red lines) in Figure 1b. Note that the collimated laser beam illuminating the turbulent layer represents a source at infinity; hence, it would be focused to a point-like ideal point-spread function (PSF) at a distance f (the telescope focal length) behind the telescope objective if the turbulence were absent, as described in [2,3]. With turbulence, the PSF is typically offset from the location of the ideal (undistorted) case due to tip-tilt effects and distorted from the ideal diffraction pattern, but it still achieves best focus at the ideal image plane of the undistorted optical field.

B. Ray-Matrix Propagation Model

Ignoring diffraction effects, the location of the conjugate plane relative to the turbulent layer can be derived using the ray-matrix model of light propagation through optical components. The ray-matrix model describes the propagation of optical ray vectors in a plane, close to the optic axis. As the simplest example, consider the propagation of a ray vector in a block of free space, as shown in Figure 2.

Consider the free-space region between $z = 0$ and $z = z_1$ to be one block in an optical system. This propagation is characterized by the following ray matrix: $\begin{bmatrix} 1 & z_1 \\ 0 & 1 \end{bmatrix}$. The ray vector may encounter another optical element at $z = z_1$, such as a thin lens, which would change the direction of propagation. In this case, the propagation of the ray vector can be described by cascading two blocks.

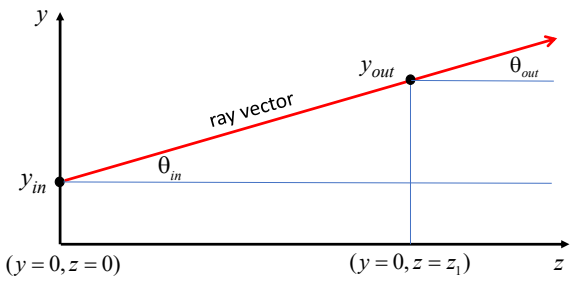

Figure 2. Ray-vector model of free-space propagation from the starting point of the free-space block at $z = 0$ to the end point at $z = z_1$.

Referring to Figure 2, we can see that the output parameters y_{out} and θ_{out} can be expressed in terms of the input parameters y_{in} and θ_{in} as follows: $y_{out} = y_{in} + z_1 \tan(\theta_{in})$ and $\theta_{out} = \theta_{in}$. These equations are exact but not linear due to the presence of the $\tan(\theta_{in})$ term. However, the equations can be made linear by applying the paraxial approximation $\theta << 1$ radian; hence, $\tan(\theta_{in}) \cong \theta_{in}$, yielding the pair of linear equations $y_{out} = y_{in} + z_1 \theta_{in}$ and $\theta_{out} = \theta_{in}$. This linearization enables the solution of complex optical systems consisting of cascaded blocks of optical components, representing lenses and other optical components.

The output of the first block is given by $\begin{bmatrix} y_{out}^{(1)} \\ \theta_{out}^{(1)} \end{bmatrix} = \begin{bmatrix} 1 & z_1 \\ 0 & 1 \end{bmatrix} \begin{bmatrix} y_{in}^{(1)} \\ \theta_{in}^{(1)} \end{bmatrix}$. Cascading two blocks typically containing different optical components can be illustrated via the following example, which also serves to highlight an important property of the ray-matrix technique. Let the propagation matrix of the first block encountered by the ray vector be denoted by $\boldsymbol{A}_1 = \begin{bmatrix} 1 & z_1 \\ 0 & 1 \end{bmatrix}$, and the second block denoted by $\boldsymbol{A}_2 = \begin{bmatrix} 1 & z_2 \\ 0 & 1 \end{bmatrix}$. Cascading the two blocks implies that the output of the first block is equal to the input to the second block; hence, $\begin{bmatrix} y_{in}^{(2)} \\ \theta_{in}^{(2)} \end{bmatrix} = \begin{bmatrix} y_{out}^{(1)} \\ \theta_{out}^{(1)} \end{bmatrix}$. The output of the cascaded system is clearly given by the fundamental cascading equation

$$\begin{bmatrix} y_{out} \\ \theta_{out} \end{bmatrix} = \boldsymbol{A}_2 \begin{bmatrix} y_{in}^{(2)} \\ \theta_{in}^{(2)} \end{bmatrix} = \boldsymbol{A}_2 \begin{bmatrix} y_{out}^{(1)} \\ \theta_{out}^{(1)} \end{bmatrix} = \boldsymbol{A}_2 \boldsymbol{A}_1 \begin{bmatrix} y_{in}^{(1)} \\ \theta_{in}^{(1)} \end{bmatrix}. \quad (1)$$

This simple example demonstrates why the propagation matrices in a cascade must be applied in reverse order: The input to the last propagation matrix is the output of the next-to-last propagation matrix, followed by the previous propagation matrix, etc. This order of multiplying propagation matrices applies to the general case, regardless of the number of blocks in the cascade and of the optical components contained within in each block.

C. Ray-Matrix Representation of the Thin Lens

Referring to the complete three-dimensional derivation in Appendix A, the ray-matrix representation of the thin lens can be derived by considering the change in the slope of the curved lens surface in the simple two-dimensional ($x = 0$, y) model shown in Figure 3:

$$\Delta(x=0,y)=\Delta_0-R\left(1-\sqrt{1-\frac{y^2}{R^2}}\right)=\Delta_0-R+R\sqrt{1-\frac{y^2}{R^2}}\cong\Delta_0-y^2/2R\ .$$

For the two-dimensional model in the $(y,\ z)$ plane shown in Figure 3, this yields the derivative

$$\frac{\partial\Delta(x=0,y)}{\partial y}=-y/R\ . \tag{2}$$

It can be seen that when $y=0$, the derivative with respect to y is zero; when $y>0$, the derivative is negative and linearly proportional to y.

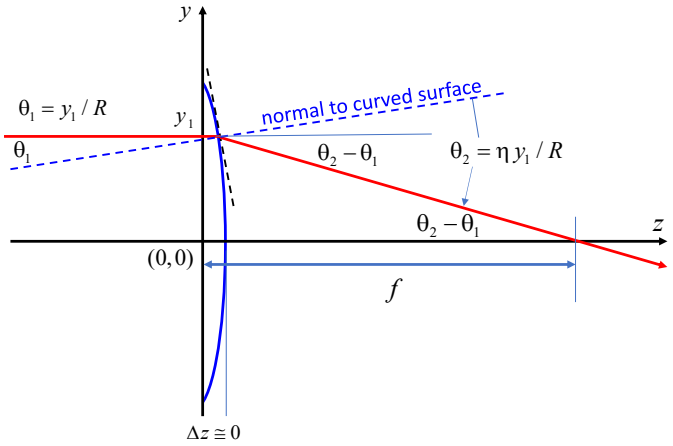

Figure 3. Illustrating the propagation and focusing of rays by a plano-convex lens, using Snell's law at the normal to the curved surface.

Referring to Figure 3, a horizontal ray enters the thin lens at coordinates at $(y=y_1, z=0)$ perpendicular to the planar surface of the thin lens; hence, there is no change in position or angle. Therefore, at an infinitesimal distance inside the planar surface of the lens, the propagation equations are $y_{out}=y_{in}$ and $\theta_{out}=\theta_{in}$; hence, the propagation matrix is $\begin{bmatrix}1 & 0\\ 0 & 1\end{bmatrix}$, yielding the ray-matrix equations $\begin{bmatrix}y_{out}\\ \theta_{out}\end{bmatrix}=\begin{bmatrix}1 & 0\\ 0 & 1\end{bmatrix}\begin{bmatrix}y_{in}\\ \theta_{in}\end{bmatrix}=\begin{bmatrix}y_{in}\\ \theta_{in}\end{bmatrix}$. Note that within each block, a ray is represented by a straight-line segment. The thin lens is considered to be a block of length zero in the ray-matrix model, since we are assuming that the extent of the thin lens along the propagation direction is essentially zero: $\Delta z\cong 0$, as shown in Figure 3.

Referring to Figure 3, it can be seen that application of Snell's law at the curved surface yields an output angle of $(\theta_2-\theta_1)$ after the incident ray intercepts the curved surface at coordinates $(y=y_1,\ z=\Delta z\cong 0)$, where $\Delta z\cong 0$ by virtue of the thin lens approximation.

Applying Snell's law to the differential area where the ray (red line) intercepts the curved surface, we have $\eta_1\sin(\theta_1)=\eta_2\sin(\theta_2)$, where (η_1,η_2) are the refractive indices inside and outside the glass, and (θ_1,θ_2) are angles measured from the normal to the surface at coordinates $(y=y_1,\ z=0)$, indicated by the dashed blue line. Denoting the refractive index inside the glass by η and outside the glass (i.e., in air) by 1 and invoking the small-angle

approximation yields $\theta_2 \cong \eta\theta_1$, where both angles are measured from the normal to the surface as shown in Figure 3.

The slope at the point $y = y_1$, where the red parallel ray shown in Figure 3 encounters the curved surface is $-y_1/R$. By application of Snell's law, $\theta_2 \cong \eta\theta_1 = -\eta y_1/R$. The angle of interest here is the angle with respect to the z-axis, or $\theta_2 - \theta_1$, which determines the intersection of the ray with the z-axis. Writing this angle as $\theta_2 - \theta_1 = -\eta\, y_1/R + y_1/R = -\frac{y_1}{R}(\eta - 1)$, and noting from Figure 3 that $\tan(\theta_2 - \theta_1) = y_1/f \cong \theta_2 - \theta_1$, we can solve for the focal length f in terms of R and η as

$$f \cong \frac{y_1}{\theta_2 - \theta_1} = \frac{y_1}{\frac{y_1}{R}(\eta - 1)} = \frac{R}{(\eta - 1)} \quad . \tag{3}$$

Note that within the limits of the paraxial approximation, f is not a function of y_1, which implies that after propagation all horizontal rays entering the thin lens intersect the z-axis at exactly the same point $z = f$, independent of y_1.

Based on this analysis, the block consisting of the thin lens between coordinates $z = 0$ and $z = \Delta z << 1$, we can write $y_{out} = y_{in}$ because the y-coordinates of the input and output are basically the same. However, the output angle changes significantly with distance from the z-axis, as can be seen in Figure 3. For the linear small-angle model, we can write $\theta_{out} = \theta_{in} - (\theta_2 - \theta_1) = \theta_{in} - \frac{y_1}{R}(\eta - 1) = \theta_{in} - \frac{y_1}{f}$. The output equations therefore become $y_{out} = y_{in}$ and $\theta_{out} = -\frac{y_1}{f} + \theta_{in}$, or in matrix form $\begin{bmatrix} y_{out} \\ \theta_{out} \end{bmatrix} = \begin{bmatrix} 1 & 0 \\ -1/f & 1 \end{bmatrix} \begin{bmatrix} y_{in} \\ \theta_{in} \end{bmatrix}$. It can be seen that the propagation matrix of the block consisting of the thin lens is of the form $\begin{bmatrix} 1 & 0 \\ -1/f & 1 \end{bmatrix}$. This propagation matrix and the free-space propagation matrix described earlier are the key building blocks for analyzing the optical system designed specifically for the JPL Mesa Adaptive Optics experiments.

D. Interpretation of Propagation Matrix Components

Based on the above examples, the four components of the propagation matrix can be understood in terms of first-order derivatives of the input and output parameters.

Recall that for the thin lens model $\Delta z \cong 0$; hence, the ray simply changes slope between the input and output planes (which have the same z-coordinate), but the y-coordinate does not change according to this linear small-angle model. However, the slope of the ray depends on the y-coordinate (where the ray intersects the input plane), as shown in Equation (2).

In homogenous media, such as a vacuum, air, or glass, with a constant refractive index, the two-dimensional outputs y_{out} and θ_{out} describing the propagation of a ray are each functions of two variables, namely y_{in} and θ_{in}, and hence can be written as $y_{out}(y_{in}, \theta_{in})$ and $\theta_{out}(y_{in}, \theta_{in})$. With the linear model, and further assuming small changes in position and

angle within each block, the outputs can be approximated in terms of total derivatives and inputs as $y_{out} = \frac{\partial y_{out}}{\partial y_{in}} y_{in} + \frac{\partial y_{out}}{\partial \theta_{in}} \theta_{in}$, and $\theta_{out} = \frac{\partial \theta_{out}}{\partial y_{in}} y_{in} + \frac{\partial \theta_{out}}{\partial \theta_{in}} \theta_{in}$.

The pair of linear equations describing the propagation of the ray vector in a free-space block can be written in matrix form as

$$\begin{bmatrix} y_{out} \\ \theta_{out} \end{bmatrix} = \begin{bmatrix} 1 & z_1 \\ 0 & 1 \end{bmatrix} \begin{bmatrix} y_{in} \\ \theta_{in} \end{bmatrix} \quad \rightarrow \quad \begin{bmatrix} y_{out} \\ \theta_{out} \end{bmatrix} = \boldsymbol{A} \begin{bmatrix} y_{in} \\ \theta_{in} \end{bmatrix} \quad \boldsymbol{A} \triangleq \begin{bmatrix} A & B \\ C & D \end{bmatrix},$$

where $\boldsymbol{A}$ is the two-dimensional propagation matrix with components (A, B, C, D), and where

$$A = \frac{\partial y_{out}}{\partial y_{in}}, \; B = \frac{\partial y_{out}}{\partial \theta_{in}}, \; C = \frac{\partial \theta_{out}}{\partial y_{in}}, \; D = \frac{\partial \theta_{out}}{\partial \theta_{in}}.$$

This form of the linearized propagation model describes the evolution of the ray vectors in terms of the input values and their partial derivatives (i.e., rates of change) within each optical block. As a heuristic explanation of the partial derivatives, the matrix element A corresponds to spatial magnification, $B = 0$ represents distance to the image, C is the negative inverse of the lens focal length f, and D is the angular magnification M typically associated with telescopes.

E. Ray-Matrix Model of Receiver Optics

A conceptual block diagram of the optical receiver designed to collect turbulence data on the JPL Mesa Test Range is shown in Figure 4. In this figure, ER refers to eye relief.

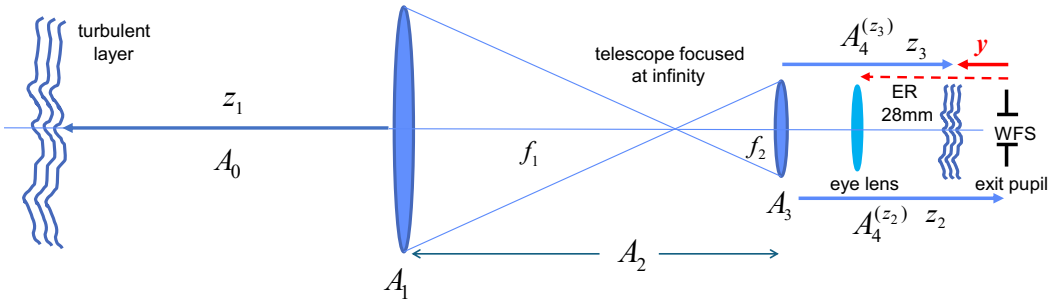

Figure 4. Optical configuration for horizontal-path tomography data collection and analysis.

In Figure 4, the turbulent layer is a distance z_1 from the telescope objective, characterized by the ray matrix $A_0 = \begin{bmatrix} 1 & z_1 \\ 0 & 1 \end{bmatrix}$ as shown above. Propagation through the objective is characterized by $A_1 = \begin{bmatrix} 1 & 0 \\ -1/f_1 & 1 \end{bmatrix}$. Similarly, $A_2 = \begin{bmatrix} 1 & f_1 + f_2 \\ 0 & 1 \end{bmatrix}$; $A_3 = \begin{bmatrix} 1 & 0 \\ -1/f_2 & 1 \end{bmatrix}$; $A_4^{(z_2)} = \begin{bmatrix} 1 & z_2 \\ 0 & 1 \end{bmatrix}$; and $A_4^{(z_3)} = \begin{bmatrix} 1 & z_3 \\ 0 & 1 \end{bmatrix}$. Applying these matrices in the correct (i.e., reverse) order, we obtain either $A^{(z_2)}$ or $A^{(z_3)}$: $A^{(z_2,z_3)} = A_4^{(z_2,z_3)} A_3 A_2 A_1 A_0$.

Our goal is to determine two distances: first, the distance from the ideal eyepiece (second lens with focal length f_2) to the exit pupil, z_2; and second, the distance from the eyepiece to the image of the turbulent layer, z_3.

1. Distance from the Eyepiece to the Exit Pupil, z_2

The exit pupil is an image of the objective lens (of focal length f_1) formed by the eyepiece when $z_1 = 0$.

The corresponding matrix reduces to the identity matrix, $A_0 = \begin{bmatrix} 1 & 0 \\ 0 & 1 \end{bmatrix}$; hence, it need not be included in the calculations. This yields the ray matrix

$$A^{(z_2)} = A_4^{(z_2)} A_3 A_2 A_1 = \begin{bmatrix} 1 & z_2 \\ 0 & 1 \end{bmatrix} \begin{bmatrix} 1 & 0 \\ -1/f_2 & 1 \end{bmatrix} \begin{bmatrix} 1 & f_1 + f_2 \\ 0 & 1 \end{bmatrix} \begin{bmatrix} 1 & 0 \\ -1/f_1 & 1 \end{bmatrix} \triangleq \begin{bmatrix} A & B \\ C & D \end{bmatrix} . \quad (4)$$

According to the condition for image formation described above, the ray-matrix component must be equal to zero, $B = 0$, because all rays must pass through the same point on the z-axis to form an image. Letting $B = 0$ yields the following solution, as shown in Appendix B-1:

$$B^{(z_2)} = (f_1 + f_2) + z_2 \left(1 - \frac{f_1 + f_2}{f_2}\right) = 0 \qquad z_2 = \frac{f_2(f_1 + f_2)}{[(f_1 + f_2) - f_2]}$$

$$z_2 = \frac{f_2(f_1 + f_2)}{f_1} = f_2(1 + f_2/f_1) \ .$$

Therefore, the distance to the exit pupil is

$$z_2 = f_2(1 + f_2/f_1) \ . \quad (5)$$

This solution shows that the image is at the focal plane of the eyepiece, $z_2 = f_2$, only if the objective is at infinity, namely if $f_1 \to \infty$.

It is informative to compare this solution to the well-known imaging equation, which is the inverse of the direct solution of Equation (5):

$$\frac{1}{z_2} = \frac{f_1}{f_2(f_1 + f_2)} = \frac{(f_1 + f_2) - f_2}{f_2(f_1 + f_2)} = \frac{1}{f_2} - \frac{1}{f_1 + f_2} \ . \quad (6)$$

This is recognized as the equation for imaging an object at a distance of $f_1 + f_2$, namely at the telescope objective from a lens with focal length of f_2.

2. Distance from Exit Pupil to Image of Turbulent Layer

Following the ray-matrix analysis for the distance to the exit pupil as explained in the preceding subsection, the distance to the image of the turbulent layer is determined next. For this case, the distance from the turbulent layer to the telescope objective is not zero but z_1; hence, the ray matrix for this case is $A_0 = \begin{bmatrix} 1 & z_1 \\ 0 & 1 \end{bmatrix}$, which is clearly not the identity matrix and therefore must be included in the ray-matrix analysis. In addition, the last ray-matrix component incorporates propagation from the idealized eyepiece lens to the image of the turbulent layer, namely $A_4^{(z_3)} = \begin{bmatrix} 1 & z_3 \\ 0 & 1 \end{bmatrix}$. The derivation of this general case is in Appendix B-2:

$$\frac{1}{z_3} = \frac{1}{f_2} - \frac{1}{[z_1/(1 - z_1/f_1)] + (f_1 + f_2)} \ . \tag{7}$$

This equation differs from the imaging equation for the exit pupil, which is the image of the objective generated by the eyepiece in Equation (10), only by the term involving the distance to the turbulent layer, z_1, in the denominator of the second term in the right-hand side of Equation (7).

For experiments designed to determine the location of the turbulent layer in the field by measuring the distance to the conjugate plane behind the eyepiece, it is useful to have a direct expression for z_3, which can be obtained by inverting the expression for $1/z_3$, after expanding and simplifying as shown in Appendix B-3:

$$z_3 = \frac{f_2}{f_1}\left((f_1 + f_2) - \frac{f_2 z_1}{f_1}\right) \ . \tag{8}$$

An interesting feature of Equation (8) is that it can be rearranged to demonstrate the inherent symmetry between conjugate planes in this optical configuration by subtracting the right-hand side from the left-hand side and setting equal to zero:

$$\frac{f_1 z_3}{f_2} - (f_1 + f_2) + \frac{f_2 z_1}{f_1} = 0 \ . \tag{9}$$

Equation (9) enables solving for either z_1 or z_3 by inspection, demonstrating that an object can be placed at either the z_1 or z_3 location, resulting in the formation of an image at the conjugate distance z_3 or z_1, respectively. For example, solving Equation (9) for z_1 yields

$$z_1 = \frac{f_1}{f_2}\left((f_1 + f_2) - \frac{f_1 z_3}{f_2}\right) \ . \tag{10}$$

Equations (8) and (10) clearly demonstrate the inherent symmetry of this physical principle. In other words, a real object of diameter D placed at z_1 produces an image of diameter D/M at the conjugate plane z_3, after propagating through the optical system of Figure 4. Similarly, a real object of diameter D/M at z_3 back-propagating through the same optical system generates an image of diameter D at its conjugate plane, namely z_1.

III. Mesa Test Range Configuration for Laser Tomography Experiments

The laser tomography experiments were conducted on the JPL Mesa Test Range, where the optical receiver was stationed in the anteroom of Building 212, and the laser transmitter was located at the "long range" distance of roughly 228 m behind the "far" heater, as shown in Figure 5. Initial system testing was carried out at a "short range" distance of roughly 70 m, where the transmitting telescope was set up on the concrete pad next to Mesa Road, closest to the anteroom of Building 212.

A laser transmitter consisting of a 650-nm diode laser, a 106-mm refracting telescope on a solid Az-El mount equipped with a projection lens to expand the laser beam to fill the transmitting telescope's objective diameter, and a focusing assembly to enable fine-tuning the divergence of the output beam directed at the receiving telescope in the anteroom.

It was found that a fully collimated (circular) 106-mm output beam saturated the WFS outputs at the receiver; hence, a slightly divergent beam had to be used for best results. The view from the transmitter toward the receiver is shown in Figure 6a, and the opposite view from the receiver to the laser transmitter is shown in Figure 6b.

Figure 5. Long-range configuration for experimental data acquisition.

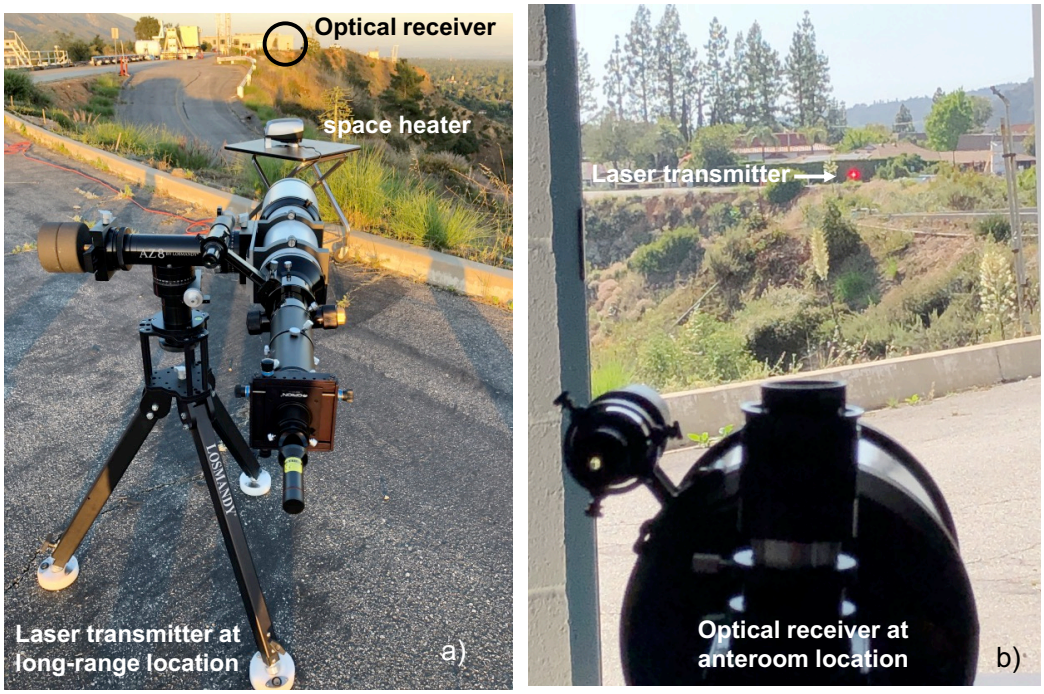

Figure 6. a) Laser transmitter telescope roughly 228 m from the receiver in the Building 212 anteroom (based on laser rangefinder distance measurements) showing 650-nm laser, x-y positioner, projection eyepiece coupler, 106-mm transmitter (refractor) telescope, space heater placed under the beam roughly 4 m from the objective, and the open door of the anteroom of Building 212; b) Celestron 125-mm optical receiver telescope in the anteroom of Building 212, collecting the red (650-nm) laser signal from the long-range location.

A. Estimating Distance to Artificial Heater-Induced Turbulent Layers

The arrangement of the optical components at the output of the receiving telescope, designed to characterize the location of the turbulent layers along the JPL Mesa Test Range, is shown in Figure 7. The telescope is a catadioptric design with 125-mm aperture and focal length of 1,250 mm, which means that a collimated beam coupled into the telescope aperture is focused to a point in the focal plane at an effective distance of 1,250 mm along the optical axis, forming a bright spot that can be photographed or viewed on a projection screen placed at the focal plane. As a heuristic explanation, a bright point-source at infinity (such as a star or a laser transmitter located a great distance from the telescope) will be focused to a small PSF in the focal plane.

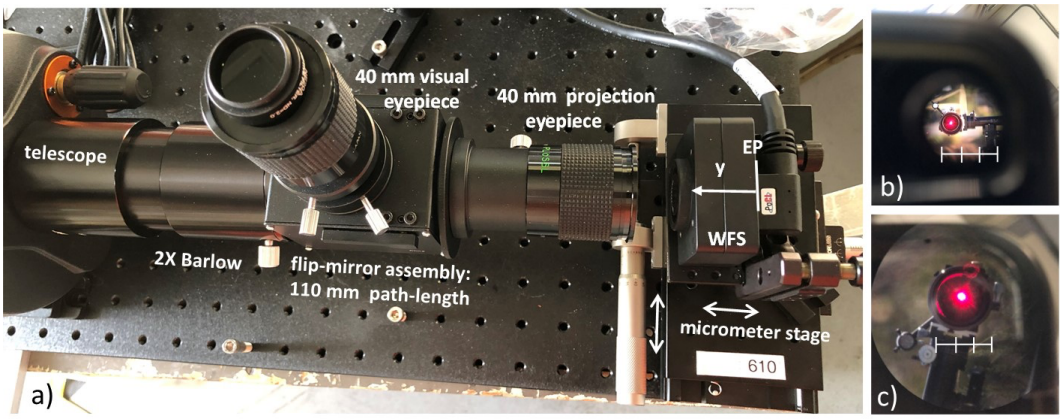

Figure 7. a) Receiver optical configuration for measuring distance to turbulent layers along the LOS; b) view of transmitter laser through the 40-mm visual eyepiece without Barlow lens; c) view of transmitter laser through the 40-mm visual eyepiece with 2X Barlow lens.

In order to view a distant object directly through the telescope, an eyepiece must be used to recollimate the diverging rays emanating from the PSF in the focal plane and match the parallel collimated rays into the pupil of the eye, where the rays are focused onto the retina by the eye lens. To couple all of the rays collected by the telescope aperture into the pupil, the diameter of the recollimated beam must be matched to the viewer's eye pupil diameter, which is typically 7 mm or less for a dark-adapted eye (depending on age). This means that a 125-mm collimated beam entering the telescope aperture must be converted to a 7-mm or smaller collimated beam by the eyepiece, requiring demagnification by a factor of $M = 125/7 = 17.8571$ or greater. Since telescope magnification is defined as the effective focal length of the telescope divided by the focal length of the eyepiece, this would require an eyepiece with a focal length of 1250/17.8571 = 70 mm, which is possible, but not practical. Higher magnifications can be obtained by using shorter-focal-length eyepieces, further reducing the diameter of the ray-bundle entering the exit pupil.

The human eye is typically placed at the telescope's exit pupil, which is an image of the telescope aperture formed by the eyepiece. This means that all the rays that pass through the telescope aperture and through the eyepiece also pass through the exit pupil (unless prevented by internal baffling or other internal obstructions). However, the diameter of the ray-bundle has been reduced by a large factor, namely by the spatial magnification $M = y_{out}/y_{in}$ as described earlier.

The effective focal length of any telescope can be increased by inserting a negative lens, called a Barlow lens (after its inventor Peter Barlow), between the telescope output and the eyepiece. Figure 7 shows a 2X Barlow coupled into the telescope output, which increases the effective focal length of the telescope by a factor of 2, from 1,250 mm to 2,500 mm. The simplest way to incorporate this into the thin lens model is to increase the focal length of the thin lens representing the receiving telescope objective.

The distance to the turbulent layer z_1 probed by the WFS, as a function of distance from the thin-lens model of the eyepiece, z_3, can be seen in Figure 8 for the case of no Barlow lens and for 2X and 3X Barlow lenses.

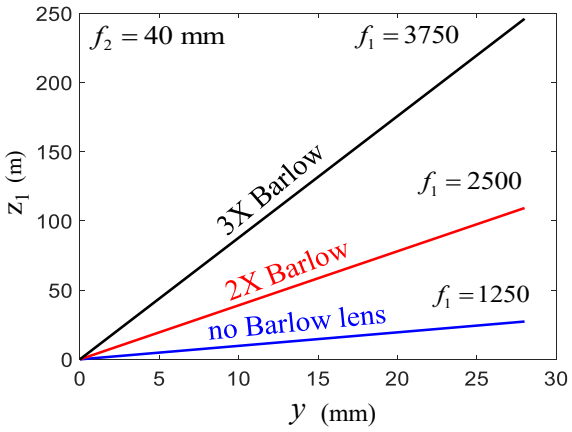

Figure 8. Examples of the probing distance to various turbulent layers, z_1, as a function of WFS distance from the exit pupil y, as shown in Figure 4.

However, the optical configuration of Figure 7a shows a flip-mirror assembly between the telescope assembly and the eyepiece, equipped with identical 40-mm Plossl eyepieces to make sure that the optical fields reaching the eye and the WFS are the same. The purpose of the flip-mirror assembly is to enable visual confirmation of the transmitter laser and make sure that the receiving telescope is focused at infinity. With a collimated laser beam, this is equivalent to seeing a bright spot centered on the objective lens of the transmitter telescope, as shown in Figures 7b and 7c.

The flip-mirror assembly adds an extra 110 mm to the pathlength between the output of the Barlow and the eye, or equivalently to the pathlength between the Barlow and the WFS. This extra pathlength increases the magnification of the Barlow, M_B, according to the following formula: $M_B = L/|f_B| + 1$, where L is the added pathlength and f_B is the effective focal length of the Barlow lens, which is a negative number. However, the negative focal lengths of Barlow lenses are typically not published; hence, this formula is not very practical.

A better approach is to measure the field of view (FOV) of the eyepiece directly. In this case, the eyepiece was a 40-mm Tele View Plossl with 43-degree apparent FOV. The approach was to set up an accurate millimeter-scale ruler some distance from a small telescope and measure the FOV across the diagonal directly through the telescope first, then with 2X and 2.5X Barlows in the optical path, followed by the 110-mm flip-mirror assembly set up exactly as in the configuration of Figure 8. The results are as follows: Without the Barlow,

the FOV across the field-stop of the eyepiece was 31 cm; with the 2X Barlow, it was 10.1 cm; and with the 2.5X Barlow, it was 8.2 cm. Based on these measurements, the true magnifications with the 2X and 2.5X Barlows were 3.07X and 3.78X, respectively.

B. Average Wavefront Errors via WFS Measurements

The collimated output of the eyepiece serves as the input to the Thorlabs WFS, model WFS20-14AR, which collects data for real-time analysis by the supplied software. The software generates CSV files containing real-time estimates of the total RMS wavefront error, along with estimates of the first 15 Zernike coefficients. The WFS is mounted on a micrometer stage with 25 mm travel and 0.0025 mm resolution.

The WFS consists of a 7.2 × 5.4-mm sensor with 5 × 5-µm pixels, 1,440 × 1,080 total pixels, and a microlens array with 300 micron pitch (295-µm lenslets), where each lenslet samples a differential area of the received phase-front so small that under typical turbulence conditions the phase-front over the lenslet is basically a plane-wave, and generates a PSF on the 60 × 60-pixel subarray directly under each lenslet element.

As an example, notice that if there is no turbulence, the lenslet will focus the captured plane-wave to a spot at the center of the 60 × 60 pixel subarray. But with turbulence present, the differential plane-wave captured by a lenslet tends to be tilted, leading to a displacement of the spot from the center, which can be measured and converted to an angle via the formula $\theta_{spot} = \rho / f_{lenslet}$, where the displacement $\rho = \sqrt{x^2 + y^2}$, (x,y) are the pixel-coordinates of the subarray, and $f_{lenslet}$ = 14.6 mm for the WFS20-14AR WFS. For example, if the average pixel displacement over all lenslets is on the order of 1 pixel, then the average measured angle is $(5 \times 10^{-6})/(14.6 \times 10^{-3}) = 3.4247 \times 10^{-4}$ radians, or roughly 0.34 milliradians. Referring the angular magnification back to the telescope aperture using M = 1250/40 = 31.25, the average error becomes $(3.4247 \times 10^{-4})/31.25 = 10.96$ µrads, which is comparable to the largest RMS errors obtained during these experiments. Examples of the spot-fields generated by the telescope-flip-mirror-WFS combination with and without a 2X Barlow lens are shown in Figure 9.

The impact of magnification on the diameter of the collimated output beam is clearly shown in Figure 9b, where the image of the aperture at the exit pupil is roughly three times smaller than without Barlow, as in Figure 9a. The estimated diameters shown in Figure 9, which differ by a factor of 12.083/4.4721 = 2.7019, imply a slightly smaller magnification than obtained with direct measurement (3.07). However, the actual diameter of the aperture image in Figure 9a is likely somewhat larger than shown, since there are additional spots on the lower left side of the circle that the software did not take into account in adjusting the diameters of the circles, which represent the area wherein the spots contributing to the RMS calculation are defined. The large, roughly 300 µm sampling grid defined by the spots naturally introduces errors in estimating the true diameter of the aperture image. For example, if the true diameter of the image is closer to 13 sample units instead of 12.083, then the implied magnification would be 2.91 instead of 2.7, which is in closer agreement with the directly measured magnification of 3.07X. In any event, the spotfield measurements serve only to validate the optical setup and do not impact the accuracy of the RMS error measurements conducted during these experiments.

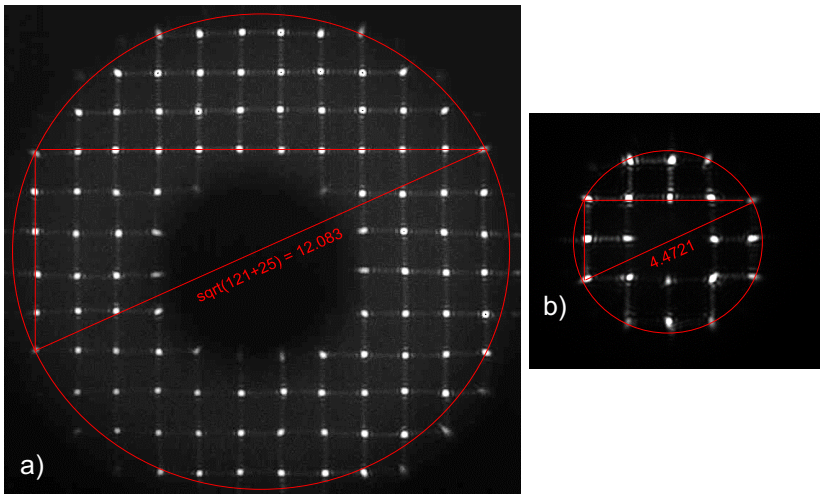

Figure 9. Examples of spotfield diagrams obtained on the JPL Mesa Test Range under good seeing conditions, showing the image of the aperture with central obstruction: a) 125-mm F/10 telescope, 1,250-mm focal length, no Barlow lens; b) same telescope, 2X Barlow with 3.07X magnification, effective focal length 3,837.5 mm.

The RMS phase errors are measured by processing the raw output data of the Thorlabs WFS20-14AR. The raw spotfield data generated by the WFS are converted to (x, y) offsets by measuring the centroid of the spot over each 60×60 detector subarray (directly under each element of the lenslet array) and further processed by Thorlabs software to extract the first 15 Zernike coefficients from the spotfield data. The first Zernike element, Z_1, is a piston term that has no impact on tip tilt (Z_2, Z_3) or on higher-order ($Z_4 - Z_{15}$) performance of an Adaptive Optics system; hence, it was not considered in the computation of RMS phase error.

The optical configuration and key equations used during the Mesa Test Range experiments are shown in Figure 10. A key parameter required for understanding the experimental data is the scale-factor estimate $\hat{S}$ relating the change in distance to the turbulent layer in the field, z_1, to the change in WFS position $y = z_2 - z_3$, which can be read directly from the micrometer scale. Note that when the field turbulence is at the telescope aperture, such that $z_1 = 0$, the real image of the turbulence (i.e., the conjugate plane) appears at the exit pupil of the eyepiece at a distance z_2.

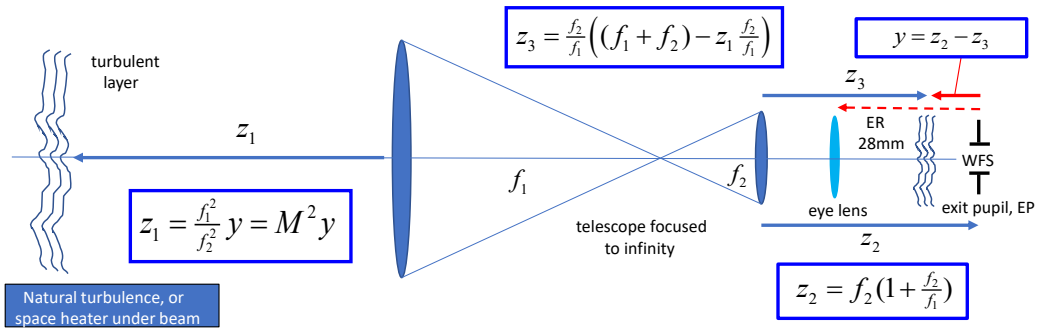

Figure 10. Optical configuration for experimental data analysis.

As the distance from the telescope aperture to the turbulent layer increases, so does the distance from the exit pupil to the conjugate plane. Therefore, the scale factor $\hat{S}$ is a positive number. From the definition, the scale factor can be calculated as $\frac{\partial z_1}{\partial y}$, by substituting for z_2, z_3 and calculating the derivative as follows:

$$z_2 = f_2\left(1+\frac{f_2}{f_1}\right) = f_2 + \frac{f_2^2}{f_1} \qquad z_3 = \frac{f_2}{f_1}\left((f_1+f_2) - \frac{f_2 z_1}{f_1}\right) = f_2 + \frac{f_2^2}{f_1} - \frac{f_2^2}{f_1^2} z_1$$

$$y = z_3 - z_2 = \frac{f_2^2}{f_1^2} z_1 \qquad z_1 = \frac{f_1^2}{f_2^2} y \qquad \frac{\partial z_1}{\partial y} = \frac{f_1^2}{f_2^2} \quad . \tag{11}$$

Several terms cancel in Equation (11); hence, the scale-factor estimate reduces to:

$$\hat{S} = \frac{\partial z_1}{\partial y} = \frac{f_1^2}{f_2^2} \ . \tag{12}$$

The reason for specifying an estimate for the scale factor instead of a true value is that f_1 and f_2 are nominal values due to the additional 110-mm gap introduced by the flip-mirror assembly, as shown in Figure 7, and by uncertainty in the manufacturer's specifications for Barlow magnifications, which can be in error by a few percent. The scale-factor estimates used to process the experimental data are shown in Table 1 for three cases: without Barlow, with 2X Barlow, and with 2.5X Barlow.

The eyepiece focal length was assumed to be exactly 40 mm as specified by the manufacturer; however, in practice the focal lengths of the amateur optics may be slightly different. The measured values for Barlow magnification, including the 110-mm gap due to the flip-mirror assembly (which is equivalent to an extension tube), are nominally 3.1X and 3.8X for the 2X and 2.5X Barlow, respectively. Note that when no Barlow is used, the specified effective focal length of the telescope does not change when the flip-mirror assembly is added, since the additional 110 mm free-space gap can be eliminated by refocusing the telescope.

Using the value for the effective focal length $\tilde{f}_1$ from Table 1, we can calculate the rate of change in the distance to the physical turbulent layer, z_1, with change in the WFS distance y, for the 2.5X Barlow used in the long-range experiments:

$$\hat{S} \triangleq \frac{\partial z_1}{\partial y} = \frac{f_1^2}{f_2^2} = \left(\frac{4.75}{0.04}\right)^2 = 14.1 \text{ m/mm} \ .$$

Table 1. Measured values of Barlow plus gap magnification M_B and scale factor $\widehat{S}$.

	f_2, mm	f_1, mm	gap, mm	M_B	$\hat{f}_1$, mm	$\widehat{S}$, m/mm
No Barlow	40	1,250	110	1	1,250	0.977
2X Barlow	40	1,250	110	3.1	3,835	9.385
2.5X Barlow	40	1,250	110	3.8	4,750	14.1

In Figure 11, the far and near heaters are located at micrometer readings of 17.145 mm and 3.175 mm, respectively. Hence, the difference is 13.97 mm. Applying the measured value of $\hat{S}$ = 14.1 m/mm, the calculated distance between heaters is $14.1 \times 13.97 = 196.977 \cong 197$ m. This value of L can also be read off directly from Figure 11, where distance has been converted to meters: $L = 241.7445 - 44.7675 = 196.977 \cong 197$ m.

Note that the blue curve in Figure 11 includes both tip-tilt and higher-order Zernike coefficients, whereas the red curve does not. This implies that the tip-tilt components introduced by the far heater (closest to the laser transmitter) propagate along the path, causing large fluctuations between the heaters, and eventually add to the tip-tilt caused by the near heater (closest to the receiver). This effect is exaggerated by the fact that the far heater was set to higher power than the near heater to account for propagation losses.

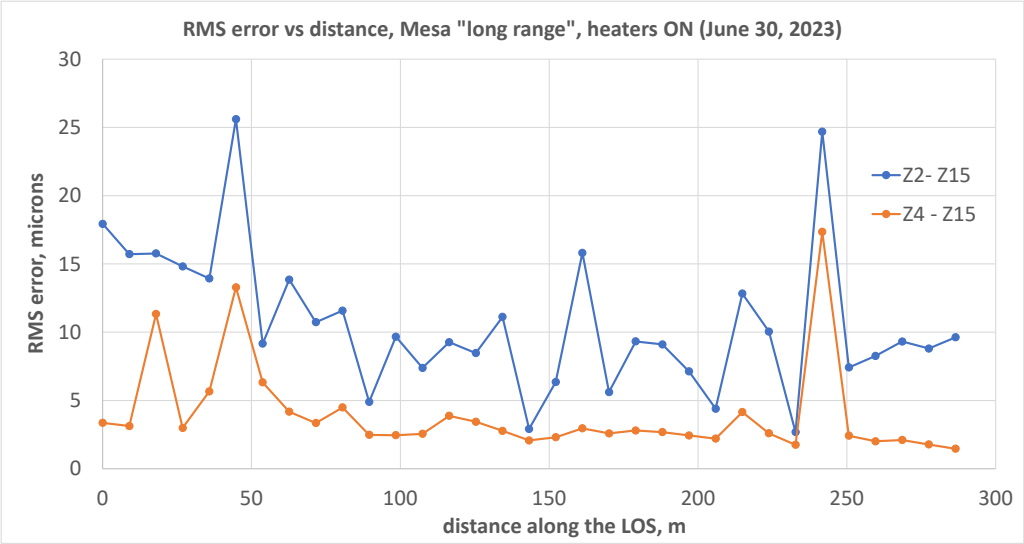

Figure 11. Results of two-heater tomography experiment conducted on June 30, 2023. Blue line: RMS error calculated using Zernike coefficients Z_2–Z_{15} (includes tip-tilt components); red line: RMS error calculated via higher-order Zernike coefficients Z_4–Z_{15} (excluding tip-tilt components).

Whereas the distance between the two dominant peaks corresponding to the locations of the near and far heaters is well defined in Figure 11, the location of the exit pupil is a rough estimate based on the bright disk (real image of the telescope objective) projected onto a white card in front of the eye-lens due to bright daylight sky. Therefore, the differential distance between heaters is used to compare the calculated distance with measured values and laser range finder estimates to validate the calculated results.

For comparison, the distance between far heater and the door to the anteroom over the long-range path was measured to be 224 m using a Leupold laser range finder (absolute accuracy specified as 1 m), and 15 m between the door to the anteroom and the curb where the near heater was located. Applying the measured 15 m distance between the near heater and the door to the anteroom, the differential distance between the two heaters is $224 - 15 = 209$ m, which differs from the calculated distance of 197 m by 12 m, or 6%. This difference could be due to optical effects that were not taken into account, such as the fact

that the transmitter beam was slightly divergent instead of fully collimated, to avoid saturating the WFS. In addition, quantizing the micrometer readings at 1/40th of an inch (or 0.635 mm) can also introduce ±4.5 m error, and small differences between the specified and actual focal lengths of the amateur optics have not been calibrated out in this analysis and would also contribute to this error. For example, if the true focal length of the amateur Plossl eyepiece was 39 mm instead of 40 mm as assumed in our calculations (representing a 2.5% error), then the scale factor would become $\hat{S} \triangleq \frac{\partial z_1}{\partial y} = \frac{f_1^2}{f_2^2} = \left(\frac{4.75}{0.039}\right)^2 = 14.834$ m/m, and the calculated distance between the near and far heaters would become $13.97 \times 14.834 = 207.23$ m, in much better agreement with the measured value of 209 m. Similarly, if the divergent laser beam caused a 2.5% increase in the effective focal length of the telescope, that would have a similar effect on the calculated distance. In both cases, the difference between measured and calculated values would be reduced to 1%.

Considering these additional unresolved error sources, the measured values are in reasonably good agreement with the calculated values, generally validating the concept of identifying the location of two widely separated turbulent layers along the LOS by determining the distance from the turbulent conjugate plane to the exit pupil via RMS phase error measurements.

C. Natural Turbulent Layers Along the LOS

An example of multiple turbulent layers generated by heating of the terrain during daytime is shown in Figure 12. Strong turbulent layers could be observed via the RMS error technique following sunset on June 30, 2023, after the background radiation subsided but the terrain was still warm due to solar heating during the day. The RMS error was measured as a function of distance, shown in Figure 12, indicating strong turbulence roughly 120–220 m from the receiver.

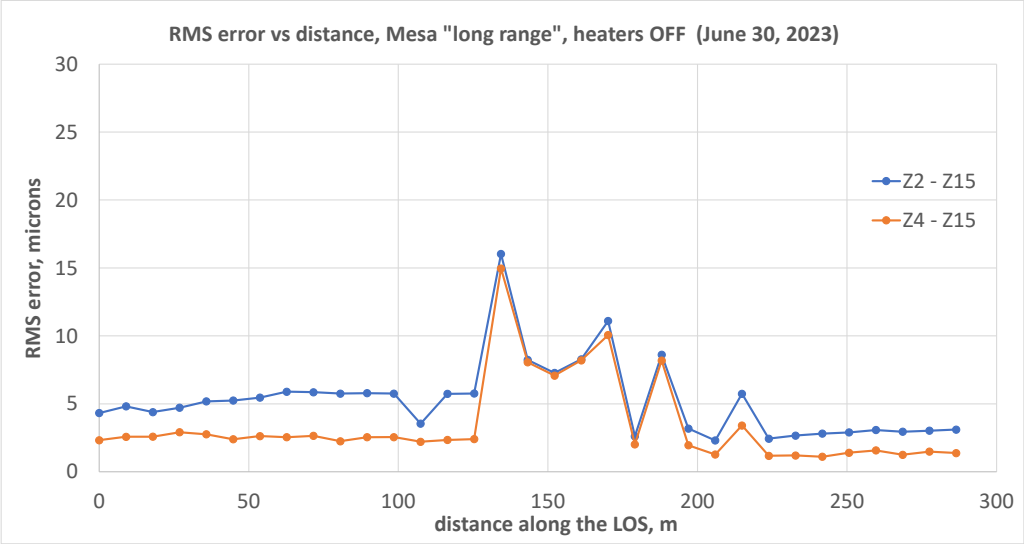

Figure 12. Results of tomography experiments characterizing natural turbulence layers along the LOS, showing well-defined RMS peaks.

The location of these naturally generated turbulence layers was superimposed on a terrain map in Figure 13, showing that large RMS errors over the receiving aperture appeared at distances corresponding to west-facing ridges along the LOS. A possible explanation for these natural turbulent peaks is that this data was taken shortly after sunset, when the west-facing sides and peaks of the ridges without much vegetation were heated more by the afternoon Sun than the east-facing ridges, generating localized thermal updraft from the warm terrain and causing turbulence, much like the heaters generated artificial turbulent layers wherever they were placed.

Figure 13. Description of long-range tomography experiment configuration, showing location of natural turbulence layers likely caused by thermal heating from the Sun.

The extreme slopes of the Mesa ridges can be clearly seen in Figure 14, which is a 3D view of the same terrain observed from the laser transmitter, in the same direction as the setting Sun when viewed from the receiver. It was also observed that natural turbulence disappeared later in the night, as the terrain cooled. This can be seen in Figure 11, where the calculated RMS error due to higher-order turbulence ($Z_4 - Z_{15}$) represented by the red curve virtually disappeared at the location of the natural peaks, even though this component was dominant earlier in the day. This observation seems to support the hypothesis that steep west-facing ridge peaks with little vegetation heated by the afternoon Sun caused natural turbulence near the center of the propagation path.

Figure 14. 3D view of the laser propagation path from Google Earth, indicating the location of natural turbulence layers, likely due to thermal heating of local peaks without much vegetation.

IV. Summary and Conclusions

The goal of this NASA-funded effort was to develop and demonstrate a practical technique for estimating the location of turbulent layers in the atmosphere along the LOS of a reference laser beam over a horizontal test path, conceptually similar to using the downlink optical signal or beacon from an interplanetary spacecraft. The idea of adjusting the location of a WFS mounted on a micrometer stage from the exit pupil of the receiving telescope (which is the conjugate plane of the telescope objective) toward the telescope eyepiece to image turbulent layers further from the objective was motivated by Figure 3 in reference [1] and the corresponding discussion therein, which provided the basis for the optical system design described in this paper. These experiments were carried out on the JPL Mesa Test Range, where the horizontal path was defined by a laser transmitter telescope near the west end of Mesa Road and a receiving telescope equipped with a Thorlabs WFS in the anteroom of Building 212.

Following detailed optical system design via ray-matrix analysis, the transmit and receive systems were set up on the JPL Mesa, and high-quality two-heater RMS-wavefront-error data was collected on June 30, 2023. With both heaters turned on, analysis of the wavefront error showed strong peaks at the nominal location of the heaters, as verified by laser rangefinder estimates of the distance between the wavefront-error peaks. In addition to artificial turbulence, natural turbulence caused by solar heating was observed and recorded shortly after sunset on June 30, providing additional data for determining turbulence peaks due to natural causes.

Future experiments will start with calibrating the optical components to accuracies greater than the nominal specified values. Following calibration, future experiments will focus on locating natural turbulent layers at non-zero elevation angles, using either stars to provide a reference signal or spacecraft with downlink beacons, such as Psyche or the Laser

Communications Relay Demonstration Mission. In addition to characterizing the range and strength of turbulent layers, efforts will be made to obtain real-time estimates of tip-tilt and higher-order wavefront errors, and apply these estimates to the laser transmitter to evaluate the effectiveness of this new technique for compensating uplink laser beams against the effects of atmospheric turbulence.

Acknowledgments

The research described in this publication was carried out by the Jet Propulsion Laboratory, California Institute of Technology, under a contract with the National Aeronautics and Space Administration.

In addition, the authors would like to thank Dimitrios Antsos for funding the initial research that led to the JPL Mesa Test Range experiment and Jason Mitchell (NASA) for funding this experiment. Many thanks to Tom Musselman and Jeff Harrell for their support of this experimental research effort on the JPL Mesa Test Range.

References

[1] J. Osborn, R. W. Wilson, V. S. Dhillon, R. Avila, and G. D. Love, "Conjugate-plane photometry: reducing scintillation in ground-based photometry," *Mon. Not. R. Astron. Soc.* vol. 411, pp. 1223–1230, 2011.

[2] J.W. Goodman, *Introduction to Fourier optics,* 2nd edition. Roberts and Company publishers, 2005.

[3] A. Fuchs, M. Tallon, J. Vernin, "Focusing on a turbulent layer," *Publication of the Astronomical Society of the Pacific* vol.110, no. 743, January 1998.

APPENDICES

Appendix A

I. Derivation of the Thin Lens Model

Referring to Figure A-1 (where the coordinate x points into the page) and paralleling the development in [2], we define the maximum thickness of the thin lens as Δ_0, leading to Equation (2) for thickness as a function of (x, y).

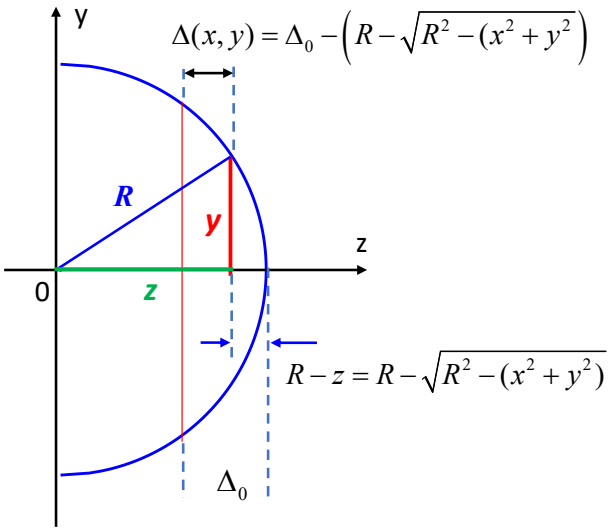

Figure A-1. Model of simple plano-convex lens used to derive the key characteristics of a thin lens.

Referring to Figure A-1, and following the development in [2], the thin lens located in the lens aperture plane can be adequately modeled for our purposes as a plano-convex spherical lens with one flat and one spherical surface. Although this is not the two-spherical-surface model discussed in [2], it is the simplest case that retains the essential features of a thin lens and therefore simplifies the analysis with no loss in generality for our purposes.

$$\Delta(x,y) = \Delta_0 - \left(R - \sqrt{R^2 - x^2 - y^2}\right) = \Delta_0 - R\left(1 - \sqrt{1 - \frac{x^2 + y^2}{R^2}}\right) . \qquad \text{(A-1)}$$

Invoking the binomial expansion for wave components near the lens axis, known as the paraxial approximation, we can rewrite the thickness function for the plano-convex thin lens as Equation (A-2):

$$\Delta(x,y) = \Delta_0 - R\left(1 - \sqrt{1 - \frac{x^2 + y^2}{R^2}}\right) = \Delta_0 - R + R\sqrt{1 - \frac{x^2 + y^2}{R^2}} \cong \Delta_0 - \frac{(x^2 + y^2)}{2R} . \qquad \text{(A-2)}$$

The thin-lens glass model assumes that a ray entering the thin-lens at coordinates (x, y) exits the thin-lens at essentially the same coordinates, after propagating a total distance Δ_0 through both glass and air. Therefore, the total propagation delay through Δ_0 at coordinates (x, y) leads to the following phase delay $\varphi(x, y)$ of Equation (A-3), as described in [2]:

$$\varphi(x,y) = k\eta\Delta(x,y) + k[\Delta_0 - \Delta(x,y)] \,, \tag{A-3}$$

where $\eta > 1$ is the refractive index of glass (roughly 1.5 for most glasses), $k\eta\Delta(x, y)$ is the phase delay through the lens, and $k[\Delta_0 - \Delta(x, y)]$ is the phase delay through air (here taken to be equivalent to vacuum).

After propagating through the thin lens, the optical field accrues an additional phase $\varphi(x, y)$, which can be expressed as the transformation of the optical field through the thin lens, $t(x, y) = \exp[j\varphi(x, y)]$, yielding the optical field just after propagating through the thin lens as $U(x, y) = t(x, y)\, U(x^-, y^-)$, where $U(x^-, y^-)$ represents the optical field just before entering the thin lens. Substituting the phase delay of Equation (A-3) into the lens transformation yields

$$\begin{aligned} t(x,y) &= \exp[-jk\eta\Delta(x,y)] \exp[-jk(\Delta_0 - \Delta(x,y)] \\ &= \exp(-jk\Delta_0) \exp[-jk\eta\Delta(x,y)] \exp[jk\Delta(x,y)] \\ &= \exp(-jk\Delta_0) \exp\{-\frac{jk}{2}(x^2 + y^2)/f\} \,, \end{aligned} \tag{A-4}$$

where the focal length f is defined as $f = R/(\eta - 1)$. The focal length f is an inherent property of the lens: It represents the distance along the z-axis where the rays of an ideal plane-wave are focused to a point, according to geometric optics. Actually, an ideal plane-wave passing through a finite aperture is focused to a PSF as described in [2], but for this application the PSF can be approximated as a mathematical point.

Appendix B

I. Derivation: Distance from the Eyepiece to the Exit Pupil, z_2

This is for the case $z_1 = 0$. Carrying out the matrix multiplication in reverse order yields the first product:

$$A_{21} \triangleq A_2 A_1 = \begin{bmatrix} 1 & f_1 + f_2 \\ 0 & 1 \end{bmatrix} \begin{bmatrix} 1 & 0 \\ -1/f_1 & 1 \end{bmatrix} = \begin{bmatrix} 1 - (f_1 + f_2)/f_1 & f_1 + f_2 \\ -1/f_1 & 1 \end{bmatrix} .$$

Similarly, the second product multiplies A_3 with A_{21}, yielding the matrix

$$A_{321} = A_3 A_{21} = \begin{bmatrix} 1 & 0 \\ -1/f_2 & 1 \end{bmatrix} \begin{bmatrix} 1 - (f_1 + f_2)/f_1 & f_1 + f_2 \\ -1/f_1 & 1 \end{bmatrix}$$

$$= \begin{bmatrix} 1 - (f_1 + f_2)/f_1 & f_1 + f_2 \\ -(1 - (f_1 + f_2)/f_1)/f_2 - 1/f_1 & 1 - (f_1 + f_2)/f_2 \end{bmatrix} .$$

The last step represents propagation over the distance z_2, yielding the matrix $A^{(z_2)}$ describing the path of the ray from objective to exit pupil:

$$A^{(z_2)} = A_4^{(z_2)} A_{321} = \begin{bmatrix} 1 & z_2 \\ 0 & 1 \end{bmatrix} \begin{bmatrix} 1 - (f_1 + f_2)/f_1 & f_1 + f_2 \\ -(1 - (f_1 + f_2)/f_1)/f_2 - 1/f_1 & 1 - (f_1 + f_2)/f_2 \end{bmatrix}$$

$$= \begin{bmatrix} 1 - (f_1 + f_2) / f_1 - z_2(1 - (f_1 + f_2) / f_1) / f_2 - z_2 / f_1 & (f_1 + f_2) + z_2(1 - (f_1 + f_2)/f_2) \\ -(1 - (f_1 + f_2) / f_1) / f_2 & 1 - (f_1 + f_2)/f_2 \end{bmatrix} ,$$

$$B^{(z_2)} = (f_1 + f_2) + z_2(1 - (f_1 + f_2)/f_2) = 0 \qquad z_2 = f_2(f_1 + f_2)/[(f_1 + f_2) - f_2)$$

$$z_2 = f_2(f_1 + f_2)/f_1 = f_2(1 + f_2/f_1) \quad ,$$

$$\frac{1}{z_2} = \frac{f_1}{f_2(f_1 + f_2)} = \frac{(f_1 + f_2) - f_2}{f_2(f_1 + f_2)} = \frac{1}{f_2} - \frac{1}{f_1 + f_2} \quad .$$

This is recognized as the imaging equation for an object at a distance of $f_1 + f_2$, namely at the telescope objective, with a collimating lens of focal length f_2.

II. Distance from Exit Pupil to Image of Turbulent Layer

For the more general case of a turbulent layer at finite distance z_1 from the telescope objective, the ray matrix is given by the product of the following component matrices:

$$A^{(z_3)} = A_4^{(z_3)} A_3 A_2 A_1 A_0 = \begin{bmatrix} 1 & z_3 \\ 0 & 1 \end{bmatrix} \begin{bmatrix} 1 & 0 \\ -1/f_2 & 1 \end{bmatrix} \begin{bmatrix} 1 & f_1 + f_2 \\ 0 & 1 \end{bmatrix} \begin{bmatrix} 1 & 0 \\ -1/f_1 & 1 \end{bmatrix} \begin{bmatrix} 1 & z_1 \\ 0 & 1 \end{bmatrix} .$$

Proceeding as in the previous subsection, the first product (in reverse order) becomes

$A_{10} \triangleq A_1 A_0 = \begin{bmatrix} 1 & 0 \\ -1/f_1 & 1 \end{bmatrix} \begin{bmatrix} 1 & z_1 \\ 0 & 1 \end{bmatrix} = \begin{bmatrix} 1 & z_1 \\ -1/f_1 & 1 - z_1/f_1 \end{bmatrix}$. The next product is

$$A_{210} \triangleq A_2 A_{10} = \begin{bmatrix} 1 & f_1 + f_2 \\ 0 & 1 \end{bmatrix} \begin{bmatrix} 1 & z_1 \\ -1/f_1 & 1 - z_1/f_1 \end{bmatrix}$$

$$= \begin{bmatrix} 1 - (f_1 + f_2)/f_1 & z_1 + (f_1 + f_2)(1 - z_1/f_1) \\ -1/f_1 & 1 - z_1/f_1 \end{bmatrix},$$

followed by

$$A_{3210} \triangleq A_3 A_{210} = \begin{bmatrix} 1 & 0 \\ -1/f_2 & 1 \end{bmatrix} \begin{bmatrix} 1 - (f_1 + f_2)/f_1 & z_1 + (f_1 + f_2)(1 - z_1/f_1) \\ -1/f_1 & 1 - z_1/f_1 \end{bmatrix}$$

$$= \begin{bmatrix} 1 - (f_1 + f_2)/f_1 & z_1 + (f_1 + f_2)(1 - z_1/f_1) \\ -(1 - (f_1 + f_2)/f_1)/f_2 - 1/f_1 & -(z_1 + (f_1 + f_2)(1 - z_1/f_1))/f_2 + 1 - z_1/f_1 \end{bmatrix}.$$

The final matrix product determines the distance from the eyepiece to the image of the turbulent layer, which is denoted by z_3:

$$A^{(z3)} \triangleq A_4^{(z_3)} A_{3210} = \begin{bmatrix} 1 & z_3 \\ 0 & 1 \end{bmatrix} \begin{bmatrix} 1 - (f_1 + f_2) / f_1 & z_1 + (f_1 + f_2)(1 - z_1 / f_1) \\ (-(1 - (f_1 + f_2) / f_1) / f_2 - 1 / f_1) & \left(-\left(z_1 + (f_1 + f_2)(1 - z_1 / f_1)\right) / f_2 + 1 - z_1 / f_1\right) \end{bmatrix} = \begin{bmatrix} A & B \\ C & D \end{bmatrix},$$

where $A = 1 - (f_1 + f_2)/f_1 - z_3((1 - (f_1 + f_2)/f_1)/f_2 + 1/f_1)$,

$B = z_1 + (f_1 + f_2)(1 - z_1 / f_1) + z_3(1 - (z_1 + (f_1 + f_2)(1 - z_1 / f_1)) / f_2 - z_1 / f_1)$,

$C = (-(1 - (f_1 + f_2) / f_1) / f_2 - 1/f_1)$, and

$D = (-(z_1 + (f_1 + f_2)(1 - z_1 / f_1)) / f_2 + 1 - z_1 / f_1)$.

The image of the turbulent layer is located a distance z_3 from the equivalent thin lens eyepiece, which can be determined by solving the equation $B^{(z_3)} = 0$ for z_3:

$$B^{(z_3)} = z_1 + (f_1 + f_2)(1 - z_1/f_1) + z_3(1 - (z_1 + (f_1 + f_2)(1 - z_1/f_1))/f_2 - z_1/f_1) = 0 \ .$$

$$z_3 = \frac{z_1 + (f_1 + f_2)(1 - z_1/f_1)}{(z_1 + (f_1 + f_2)(1 - z_1/f_1))/f_2 - (1 - z_1/f_1)}$$

$$\frac{1}{z_3} = \frac{(z_1 + (f_1 + f_2)(1 - z_1/f_1))/f_2 - (1 - z_1/f_1)}{z_1 + (f_1 + f_2)(1 - z_1/f_1)}$$

$$\frac{1}{z_3} = \frac{(z_1 + (f_1 + f_2)(1 - z_1 / f_1)) / f_2}{z_1 + (f_1 + f_2)(1 - z_1 / f_1)} - \frac{(1 - z_1 / f_1)}{z_1 + (f_1 + f_2)(1 - z_1 / f_1)}$$

$$= \frac{1}{f_2} - \frac{1}{[z_1/(1 - z_1 / f_1)] + (f_1 + f_2)} \quad .$$

III. Derivation: Location of the Conjugate Plane Behind the Eyepiece, z_3

$$\frac{1}{z_3} = \frac{1}{f_2} - \frac{1}{\frac{z_1}{(1 - z_1/f_1)} + (f_1 + f_2)} = \frac{\frac{z_1}{(1 - z_1/f_1)} + f_1}{f_2\left(\frac{z_1}{(1 - z_1/f_1)} + f_1 + f_2\right)}$$

$$z_3 = \frac{f_2\left(\left[\frac{z_1}{(1 - z_1/f_1)} + f_1\right] + f_2\right)}{\left[\frac{z_1}{(1 - z_1/f_1)} + f_1\right]} = f_2 + \frac{f_2^2}{\left[\frac{z_1}{(1 - z_1/f_1)} + f_1\right]} = f_2 + \frac{f_2^2(1 - z_1/f_1)}{[z_1 + (1 - z_1/f_1)f_1]} \quad .$$

$$z_3 = f_2 + \frac{f_2^2(1 - z_1/f_1)}{z_1 + f_1 - z_1} = f_2 + \frac{f_2^2(1 - z_1/f_1)}{f_1} = \frac{f_2 f_1}{f_1} + \frac{f_2^2}{f_1} - \frac{f_2^2 z_1}{f_1^2} = \frac{f_2}{f_1}\left(f_1 + f_2 - \frac{f_2 z_1}{f_1}\right)$$

$$z_3 = \frac{f_2}{f_1}\left((f_1 + f_2) - \frac{f_2 z_1}{f_1}\right) \quad .$$

This is the solution for the distance from the idealized eyepiece lens to the location of the conjugate layer.